Materials & Design 265 (2026) 115920

Contents lists available at ScienceDirect

Materials & Design

journal homepage: www.elsevier.com/locate/matdes

Improved oxidation resistance of B-overstoichiometric $Hf_{0.33-x}Al_xB_{0.67+y}$ compared to $Ti_{0.33-x}Al_xB_{0.67+y}$ thin films: The role of point defects on grain boundary composition

Sameer Aman Salman [a,*,1], Pauline Kümmerl [a,1], Sebastian Lellig [a,b], Amir Hossein Navidi Kashani [a], Devi Janani Ramesh [a], Eva B. Mayer [a], Stanislav Mráz [a], Marcus Hans [a], Daniel Primetzhofer [c], Szilárd Kolozsvári [d], Peter Polcik [d], Johann Michler [b], Jochen M. Schneider [a]

[a] Materials Chemistry, RWTH Aachen University, Kopernikusstr. 10, D-52074 Aachen, Germany
[b] Empa, Swiss Federal Laboratories for Materials Science and Technology, Laboratory for Mechanics of Materials and Nanostructures, Feuerwerkerstrasse 39, CH-3602 Thun, Switzerland
[c] Department of Physics and Astronomy, Uppsala University, Regementsvägen 10, S-75120 Uppsala, Sweden
[d] Plansee Composite Materials GmbH, Siebenbürgerstr. 23, D-86983 Lechbruck am See, Germany

A B S T R A C T

Oxidation of B-overstoichiometric $Hf_{0.13}Al_{0.18}B_{0.69}$ and B-understoichiometric $Hf_{0.13}Al_{0.23}B_{0.64}$ films at 700 °C reveals that both compositions form Al-rich and passivating oxide scales. The superior oxidation resistance of $Hf_{0.13}Al_{0.18}B_{0.69}$ compared to previously reported B-overstoichiometric $Ti_{0.10}Al_{0.19}B_{0.71}$ films is attributed to the absence of B-enrichment at grain boundaries, as evidenced by STEM-EDX mapping.

These observations align with *ab initio* calculations, predicting that excess B in $Hf_{0.13}Al_{0.18}B_{0.69}$ is preferentially incorporated into the lattice as point defects. Formation energies of Al vacancies, transition metal vacancies, and B interstitials are lower on average in the Hf-based system by 43%, 9%, and 19%, respectively. The most plausible scenario involves the formation of Al vacancies, which, among the considered defects, display the lowest energetic barrier and best agreement with experimental lattice parameter data. Consequently, Hf-based films can accommodate higher B concentrations within the grain lattice without developing B-rich grain boundaries, in contrast to Ti-based overstoichiometric films. This significantly improves the processability of Hf-based diboride films by easing the need for strict control of the B-to-metal ratio during synthesis.

1. Introduction

Transition metal diborides (TMB_2) are characterized by alternating layers of metal and boron atoms, featuring a mix of metallic TM-TM bonds as well as ionic–covalent TM-B and B-B bonds [1]. Their high electrical conductivity [2] and thermal conductivity [3] coupled with excellent thermal stability has motivated research exploring their potential as epitaxial contact layers on semiconductors [4] and diffusion barriers in Cu interconnects [5].

For hard and wear-resistant protective coatings on cutting tools, a balance of chemical stability and mechanical properties is crucial. Group IV TMB_2 (TM = Ti, Zr, and Hf) are of interest here due to their ability to form passivating oxide scales at temperatures lower than 1000 °C in the bulk state [6–8], which is above the application temperature for cutting tools [9]. These scales consist of a glassy B_2O_3 film on top of a porous TMO_2 skeleton with liquid B_2O_3 filling the pores [7]. However, a markedly lower oxidation resistance is reported in sputter-deposited TiB_2 coatings. For example, Dorri et al. [10] reported a linearly growing porous oxide scale at 400 °C, consisting exclusively of Ti and O for a $TiB_{2.5}$ coating. Similar behaviour has been reported for a $TiB_{2.4}$ coating at 700 °C [11] and a $TiB_{2.7}$ coating at 400 °C [12]. The poor oxidation resistance of sputter-deposited TiB_2 coatings is generally attributed to their microstructure, featuring TiB_2 nanocolumns encapsulated in glassy B-rich column boundaries, which accommodate the overstoichiometric B [13,14]. Bakhit et al. [11] attributed the porous oxide scale to the evaporation of B_2O_3 at these boundaries, while Thörnberg et al. [12] introduced the idea that boric and/or metaboric acid could additionally be formed upon reaction with moisture present

* Corresponding author.
E-mail address: salman@mch.rwth-aachen.de (S.A. Salman).
[1] both authors contributed equally.

https://doi.org/10.1016/j.matdes.2026.115920
Received 16 December 2025; Received in revised form 23 February 2026; Accepted 25 March 2026
Available online 25 March 2026
0264-1275/© 2026 The Author(s). Published by Elsevier Ltd. This is an open access article under the CC BY license (http://creativecommons.org/licenses/by/4.0/).

in ambient air at these B-rich boundaries during oxidation, which is also proposed in the oxidation model by Dorri et al. [10].

Alloying the metal sites in TiB_2 and HfB_2 with Al has been shown to improve oxidation resistance in both systems via the formation of Al-enriched passivating scales [11,15–17]. $Ti_{0.33-x}Al_xB_{0.67\pm y}$ coatings with $x = 0.19 - 0.24$ show apparent similarity to TiB_2 in terms of the sensitivity of oxidation behaviour to B concentration [17]. B-stoichiometric and B-understoichiometric $Ti_{0.33-x}Al_xB_{0.67-y}$ coatings with a similar fraction of Al in the metal sublattice form scales that are both denser and thinner (~40 nm) than those on B-overstoichiometric coatings (~200 nm) after 8 h of oxidation at 700 °C [17]. On the other hand, the oxidation resistance at 700 °C of the B-overstoichiometric $Hf_{0.11}Al_{0.20}B_{0.69}$ coating reported in [15], as well as the oxide scale morphology and composition, is comparable to stoichiometric $Ti_{0.12}Al_{0.21}B_{0.67}$ coatings from Ref. [17]. This observation is significant for practical coating applications, as avoiding B-overstoichiometry when sputtering from compound TMB_2 or composite TM-B targets is challenging due to the B-enriched flux along the target normal [18]. Neidhardt et al. [18] demonstrated that sputtered Ti-B coatings match the composition of the compound target only under high deposition pressures and/or large substrate-target distances. However, these conditions lead to reduced deposition rates and less dense morphologies due to the increased thermalization of the sputtered flux [19]. In order to grow stoichiometric and understoichiometric TiB_2 coatings, Thörnberg et al. [20] used high-power pulsed magnetron sputtering (HPPMS). Navidi et al. demonstrated that precise control of the B/(Ti + Al) ratio in B-understoichiometric [17], B-stoichiometric [16,17], and B-overstoichiometric [17] $Ti_{0.33-x}Al_xB_{0.67\pm y}$ coatings can be achieved through co-sputtering using Ti–Al composite and elemental B targets. However, co-sputtering requires a more complex deposition set-up, including substrate rotation and radio-frequency power for the insulating elemental B target [17], while HPPMS similarly requires specialized power supplies and suffers from lower deposition rates [21].

In this study, we investigate the oxidation resistance at 700 °C of B-overstoichiometric $Hf_{0.13}Al_{0.18}B_{0.69}$ and B-understoichiometric $Hf_{0.13}Al_{0.23}B_{0.64}$ thin films and demonstrate the formation of dense and passivating oxide scales for both compositions. To understand the reason for the different behaviour compared to B-overstoichiometric $Ti_{0.33-x}Al_xB_{0.67+y}$ coatings [17], we investigate the grain boundary compositions in the as-deposited state by high-resolution EDX mapping. Our observations indicate differences in how B-overstoichiometry is accommodated in the $Ti_{0.33-x}Al_xB_{0.67+y}$ and $Hf_{0.33-x}Al_xB_{0.67+y}$ coatings, consistent with *ab initio* calculations of defect formation energies.

2. Methods

$Hf_{0.33-x}Al_xB_{0.67\pm y}$ films were synthesized by direct current magnetron sputtering in a high-vacuum laboratory–scale deposition chamber with a base pressure lower than 10^{-5} Pa using one HfB_2 (99.8% purity) and one AlB_2 (99.8% purity) compound target (Plansee Composite Materials, Germany) along with an elemental Al target.

$Ti_{0.33-x}Al_xB_{0.67\pm y}$ films were synthesized in another high-vacuum laboratory–scale deposition chamber with a base pressure lower than 10^{-4} Pa. One $Ti_{0.4}Al_{0.6}$ target (Plansee Composite Materials, Germany) was sputtered with a direct current power supply, while two B targets, with a purity of 99.9% (MaTeck, Germany) were sputtered with a radio frequency power supply (13.56 MHz).

All films were grown on rotating 10 × 10 × 0.5 mm α-Al_2O_3 (0001) or Si (100) substrates (Crystal GmbH, Germany) mounted at a distance of 10 cm from the target surfaces. All substrates were heated during deposition to a temperature of 400 °C. Ar was used as the working gas, with a deposition pressure of 0.6 Pa. The venting temperature was < 50 °C to minimize surface chemistry modifications by atmospheric exposure.

The power densities at the targets, substrate potentials as well as resulting deposition rates and film thicknesses are listed in Table 1 and Table 2 for $Hf_{0.33-x}Al_xB_{0.67\pm y}$ and $Ti_{0.33-x}Al_xB_{0.67\pm y}$, respectively. All films are denoted by their compositions as measured by time-of-flight elastic recoil detection analysis (ToF-ERDA or simply ERDA), with the atomic fraction of each element in the subscript. These compositions are normalized, neglecting oxygen, which was measured to be < 1.5 at.% in all films. A maximum relative systematic measurement uncertainty of 5% was considered for B, and aliquot fractions thereof for the metals, as in our previous work [15,17]. It is emphasized that these measurement uncertainties account for systematic uncertainties which originate from the detection efficiency < 1 for light elements. However, the sets of $Hf_{0.33-x}Al_xB_{0.67\pm y}$ and $Ti_{0.33-x}Al_xB_{0.67\pm y}$ films were characterized by ERDA under identical measurement conditions, without changes in hardware. Thus, it is a reasonable first-order assumption that the systematic uncertainties are identical for the $Hf_{0.33-x}Al_xB_{0.67\pm y}$ and $Ti_{0.33-x}Al_xB_{0.67\pm y}$ films. Therefore, when comparing film compositions within each system, only the statistical measurement uncertainties (count rate error) derived from the depth profiles are relevant. These uncertainties amount to ≤ 2.0 at.% for the Hf-based coatings and ≤ 0.2 at.% for the Ti-based coatings, which are smaller than the composition differences between the here discussed coatings. ToF-ERDA was performed at the Tandem Accelerator Laboratory of Uppsala University [22] to obtain the depth-resolved chemical composition of the as-deposited films. A primary ion beam of 36 MeV $^{127}I^{8+}$ projectiles was used to generate the recoils and time-energy coincidence spectra were recorded with a detector telescope, equipped with thin carbon foils for ToF measurement and a gas detector for energy discrimination [23]. As in our previous work [15], the composition of Hf-based films was quantified using data from the near-surface region of the depth profile to prevent the influence of multiple scattering events [24,25].

The structural analysis for as-deposited and oxidized samples was carried out by X-ray diffraction (XRD) using an Empyrean (Malvern Panalytical Ltd., the Netherlands) diffractometer operated in the Bragg-Brentano geometry, with an omega offset of 2° to avoid the high-intensity reflex from the single-crystal substrate. Cu K_α radiation (λ = 1.54 Å) was used as the X-ray source, which was operated at 40 kV and 40 mA, with a Ni K_β filter in the incident beam path.

Oxidation experiments were carried out in ambient air at 700 °C for exposure times of 1, 4, and 8 h using a tube furnace (F40–200/13 GERO). The as-deposited samples were placed into an inert crucible with an attached Ni/Ni-Cr thermocouple, transferred into the pre-heated furnace at 700 °C and immediately removed from the furnace after the exposure time.

A Helios NanoLab 600 (FEI Company, United States) dual-beam scanning electron microscope (SEM) and focused ion beam (FIB), equipped with a Ga^+ source, was used to extract lamellae for imaging by scanning transmission electron microscopy (STEM), using a standard trench-milling and lift-out procedure. Final thinning and polishing was done at 5 kV using a Lyra FIB/SEM system (TESCAN Group, Czech

Table 1
Deposition parameters for $Hf_{0.33-x}Al_xB_{0.67\pm y}$ films.

Film composition	HfB_2 power density [W/cm^2]	AlB_2 power density [W/cm^2]	Al power density [W/cm^2]	Substrate potential [V]	Deposition rate [nm/min]	Film thickness [μm]
$Hf_{0.13}Al_{0.23}B_{0.64}$	6	7.5	0.75	floating	21.7	1.3
$Hf_{0.13}Al_{0.18}B_{0.69}$	6	7.5	0.5	floating	18.3	1.1
$Hf_{0.15}Al_{0.11}B_{0.74}$	6	5.75	0	floating	14.9	1.1

Table 2
Deposition parameters for $Ti_{0.33-x}Al_xB_{0.67\pm y}$ films.

Film composition	$Ti_{0.4}Al_{0.6}$ power density [W/cm^2]	B power density [W/cm^2]	Substrate potential [V]	Deposition rate [nm/min]	Film thickness [μm]
$Ti_{0.13}Al_{0.22}B_{0.65}$	2	9	−100	7.3	1.3
$Ti_{0.10}Al_{0.19}B_{0.71}$ [17]	2	10	floating	8	1.4
$Ti_{0.12}Al_{0.19}B_{0.69}$	2	10	−100	6.7	0.8

Republic). The STEM cross-sectional images of the oxidized films along with the plan-view images and energy dispersive X-ray spectroscopy (EDX) maps of the as-deposited films were recorded in a Titan Themis 200 G3 (Thermo Fisher Scientific Inc., USA) with a SuperX detector for EDX mapping.

Density functional theory (DFT) [26], as implemented in the Vienna *ab-initio* simulation package (VASP), was used to calculate the formation energy of lattice defects. The basis functions used to represent the electronic wave function were generated using the projector-augmented wave (PAW) method [27–29]. Exchange and correlation were treated by the Perdew-Burke-Ernzerhof (PBE) parametrization of the generalized gradient approximation (GGA) [30]. A plane-wave kinetic energy cut-off of 500 eV was used along with a force convergence criterion of 0.01 eV/Å. The Brillouin zone was integrated using a k-point mesh of 3 × 3 × 3, generated by the Monkhorst-Pack scheme [31]. A 3 × 3 × 3 supercell consisting of 81 atoms was used to simulate the different compositions, in which the metal lattice was populated using the special quasirandom structures (SQS) method as implemented in *sqsgenerator* [32].

To calculate the energies of isolated charge-neutral lattice defects, vacancies and interstitials were introduced into the supercell by removing and/or adding an atom from/to an arbitrary lattice site. The formation energies E^{form}_{defect} of these defects were calculated using

$$E^{form}_{defect} = E^{tot}_{defect} - E^{tot}_{pristine} - \sum n_i\mu_i$$

where E^{tot}_{defect} and $E^{tot}_{pristine}$ refer respectively to the total energies of the defected and pristine supercells, n_i refers to the number of atoms of species i added or removed ($n_i > 0$ or < 0 respectively), and μ_i refers to the chemical potential of species i, which was taken to be equal to the energy per atom of i in its ground-state crystal structure. Our supercell size of 81 atoms is sufficiently large to avoid defect-defect interactions since our supercells contain only a single defect. Therefore, the computation of defect formation energies is not affected by our supercell size.

3. Results and discussion

The chemical compositions of the as-deposited thin films, measured by ERDA, are presented in Table S1 along with the associated systematic and statistical uncertainties. For $Ti_{0.33-x}Al_xB_{0.67}$ films, it has been shown that an Al atomic fraction $x \leq 0.15$ leads to the formation of a porous and non-passivating oxide scale [16]. Therefore, in this study, Hf-based films to investigate oxidation kinetics were grown with $x \geq 0.18$. To study the influence of the B stoichiometry on the oxidation resistance of these films, the power supplied to the elemental Al target was varied, resulting in B–understoichiometric films with 64.0 ±2.0 at. % B and B–overstoichiometric films with 68.9 ±1.4 at. % B. It is emphasized that these uncertainty margins represent the statistical measurement uncertainties of ERDA, see Table S1. When comparing film compositions within each material system, only the statistical measurement uncertainties, represented by the count rate errors derived from the depth profiles are relevant, as the systematic measurement uncertainties are assumed to be identical for measurements within one material system. As the statistical measurement uncertainties amount to ≤ 2.0 at.%, the variation of B concentration between $Hf_{0.13}Al_{0.23}B_{0.64}$ and $Hf_{0.13}Al_{0.18}B_{0.69}$ is significant, see Table S1.

XRD patterns in Fig. S1 show that the as-deposited Hf-based films formed a solid solution in the hexagonal AlB_2 structure (space group $P6/mmm$). While the B-overstoichiometric $Hf_{0.13}Al_{0.18}B_{0.69}$ is XRD phase-pure, B-understoichiometric $Hf_{0.13}Al_{0.23}B_{0.64}$ exhibits an additional low-intensity peak that may correspond to AlB_{12} (space group $P4_12_12$). Plan-view STEM imaging of near-surface regions (Fig. S2) indicates that the B-understoichiometric $Hf_{0.13}Al_{0.23}B_{0.64}$ film is more porous than the $Hf_{0.13}Al_{0.18}B_{0.69}$ film with a similar near-surface grain size.

After oxidation at 700 °C for 8 h (Fig. S3), no additional oxide peaks are detected by XRD, indicating an X-ray amorphous oxide scale. Fig. 1 depicts STEM micrographs in high angle annular dark field (HAADF) mode as well as EDX maps and line scans of $Hf_{0.13}Al_{0.23}B_{0.64}$ and $Hf_{0.13}Al_{0.18}B_{0.69}$ after oxidation for 8 h. $Hf_{0.13}Al_{0.23}B_{0.64}$ and $Hf_{0.13}Al_{0.18}B_{0.69}$ form chemically indistinguishable Al-rich oxide scales with thicknesses of 35 ± 9 and 36 ± 7 nm, respectively. While $Hf_{0.13}Al_{0.18}B_{0.69}$ oxidizes exclusively at the surface, oxidation also occurs along the underdense column boundaries in $Hf_{0.13}Al_{0.23}B_{0.64}$, indicated by an Al and O enrichment, as reported for stoichiometric $Ti_{0.12}Al_{0.21}B_{0.67}$ films [33].

Navidi et al. [17] compared the oxidation behavior of a $Ti_{0.13}Al_{0.24}B_{0.63}$ and $Ti_{0.10}Al_{0.19}B_{0.71}$ film at 700 °C and reported that the B-overstoichiometric film formed an approximately 6 times thicker and significantly more porous scale. Other studies on overstoichiometric Ti-B-based films, oxidized at comparable temperatures, report similar scale morphologies, which are attributed by the authors to the evaporation of B_2O_3 [11] or (meta)boric acid [10,12] formed at B-enriched grain boundaries.

Comparing scale growth kinetics of the above-discussed Hf-based films with those of Navidi et al. [17] in Fig. 2 reveals that $Hf_{0.13}Al_{0.23}B_{0.64}$ is indistinguishable from $Ti_{0.13}Al_{0.24}B_{0.63}$ in terms of the oxide scale growth kinetics at 700 °C. However, there are substantial differences for B-overstoichiometric films. The oxide scale thickness of overstoichiometric $Hf_{0.13}Al_{0.18}B_{0.69}$ after 8 h is 36 ± 7 nm, identical to the previously mentioned B-understoichiometric coatings, while that of $Ti_{0.10}Al_{0.19}B_{0.71}$ is 204 ± 16 nm. This large difference suggests that the grain boundaries of the Hf-based film might not show B-enrichment.

To identify the reasons underlying the different thicknesses and morphology of the oxide layers formed on the $Hf_{0.13}Al_{0.18}B_{0.69}$ and $Ti_{0.10}Al_{0.19}B_{0.71}$ [17] films, we analyzed the chemical composition of the grain boundaries in the as-deposited condition by EDX mapping. For a more thorough comparison, the same analysis was also performed on a Hf-based film with higher B content ($Hf_{0.15}Al_{0.11}B_{0.74}$) and a Ti-based film with lower B content ($Ti_{0.12}Al_{0.19}B_{0.69}$). Fig. 3 and Fig. 4 respectively present EDX maps and line scans of the overstoichiometric films. EDX mapping was also performed on understoichiometric $Hf_{0.13}Al_{0.23}B_{0.64}$ and $Ti_{0.13}Al_{0.22}B_{0.65}$ films and is presented in Fig. S4. The chemical compositions and XRD patterns of the Ti-based films are given in Table S1 and Fig. S5, respectively.

EDX mapping shows that in B-deficient $Hf_{0.13}Al_{0.23}B_{0.64}$ (Fig. S4a), the grain boundaries are slightly Al and O-enriched, while triple junctions show strong segregation of Al. B-deficient $Ti_{0.13}Al_{0.22}B_{0.65}$ (Fig. S4b), shows similarly Al and O-enriched grain boundaries, but the strong segregation of Al at triple junctions is not present. This similar chemical segregation in B-understoichiometric $Ti_{0.33-x}Al_xB_{0.67-y}$ and $Hf_{0.33-x}Al_xB_{0.67-y}$ films is consistent with the similar oxidation behavior at 700 °C.

Comparing first the overstoichiometric $Ti_{0.12}Al_{0.19}B_{0.69}$ and

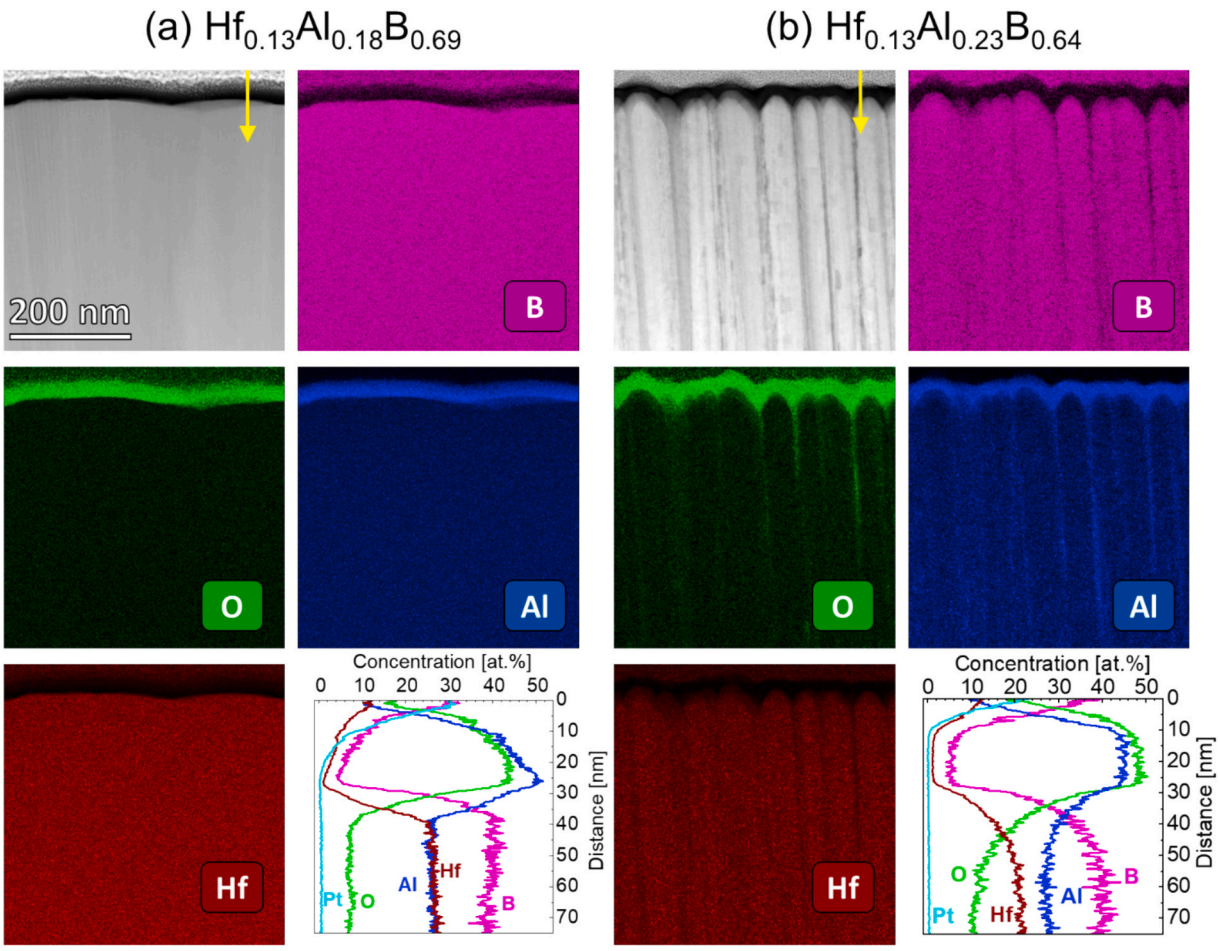

Fig. 1. Cross-sectional HAADF-STEM images, EDX maps, and EDX line scans of the oxide scale and remaining film of (a) $Hf_{0.13}Al_{0.18}B_{0.69}$ and (b) $Hf_{0.13}Al_{0.23}B_{0.64}$ after oxidation at 700 °C for 8 h. EDX line scans were performed along the arrows drawn in the corresponding HAADF-STEM micrographs.

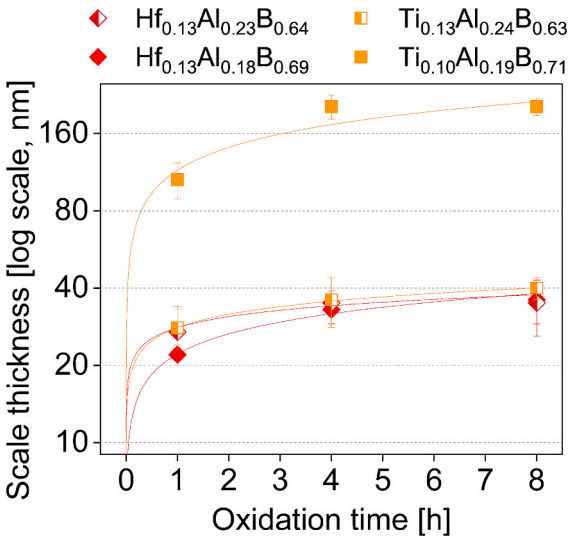

Fig. 2. Oxide scale thickness as a function of oxidation time at 700 °C for understoichiometric and overstoichiometric $Hf_{0.33-x}Al_xB_{0.67\pm y}$ (this work) as well as $Ti_{0.33-x}Al_xB_{0.67\pm y}$ [17] films. The lines are a power law fit to the data according to [34].

$Hf_{0.13}Al_{0.18}B_{0.69}$ films with 69 at.% B reveals that while the grain boundaries of $Ti_{0.12}Al_{0.19}B_{0.69}$ (Fig. 3c and 4c) are significantly enriched in B and O as well as depleted in Al and Ti, $Hf_{0.13}Al_{0.18}B_{0.69}$ (Fig. 3a and 4a) shows only minor Al enrichment and Hf depletion at the grain boundaries with no pronounced B or O segregation. $Ti_{0.10}Al_{0.19}B_{0.71}$ [17] (Fig. 3d and 4d) shows B and O enrichment at the grain boundaries similar to $Ti_{0.12}Al_{0.19}B_{0.69}$, but with enhanced magnitude. A significantly higher B content of 74 at.% in $Hf_{0.15}Al_{0.11}B_{0.74}$ (Fig. 3b and 4b) leads to similar segregation behavior as in the Ti-based films.

The above presented data suggests that B segregation at the grain boundaries is induced at higher B contents in B-overstoichiometric Hf-based films and that a greater degree of stoichiometric deviation can be accommodated in the lattice in comparison to Ti-based films. The absence of B segregation at the grain boundaries and the formation of dense oxide scales at 700 °C in $Hf_{0.13}Al_{0.18}B_{0.69}$ supports the notion that the grain boundary composition plays a key role in the oxidation behaviour.

B-overstoichiometric Hf-based films may accommodate excess B through lattice defects, thereby suppressing the formation of B-rich grain boundaries. To test this hypothesis, we calculated defect formation energies using DFT, modelling the solid solution using supercells with concentrations of $Hf_{0.12}Al_{0.21}B_{0.67}$ and $Ti_{0.12}Al_{0.21}B_{0.67}$, respectively. We focused on metal vacancies and B interstitials as the most plausible hosts for excess B. The B interstitial site was chosen at the hexagon centre within the B layer (Fig. 5b). Generally, defect formation energies in solid solutions depend on the local chemical environment [35,36]. Here, this effect is captured by plotting formation energies against the number of Al atoms in the first metal-containing coordination shell of the removed or added species, as illustrated in Fig. 5a and 5b. The range of coordination environments sampled reflects the stochastic site occupancies in each supercell.

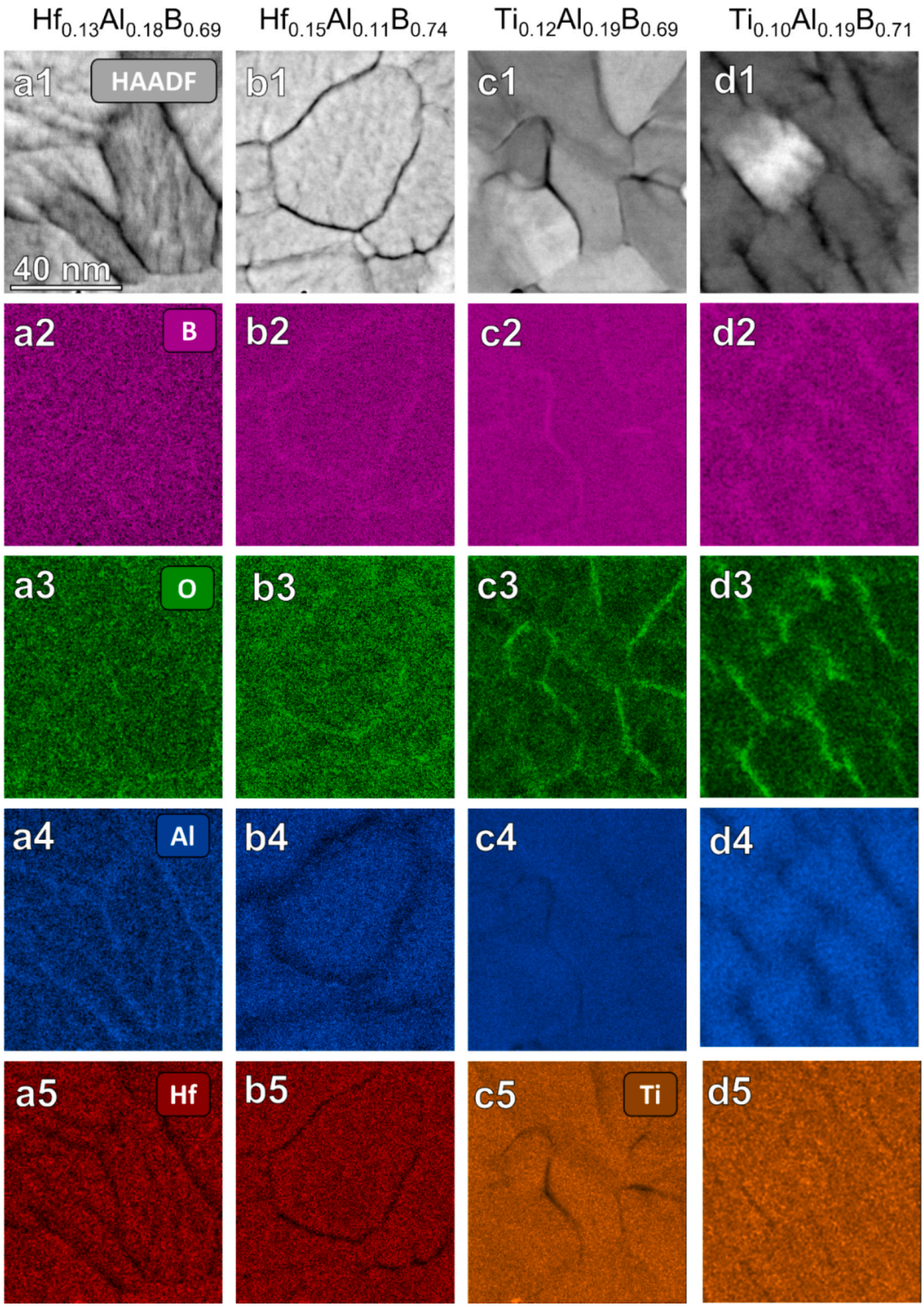

Fig. 3. STEM-HAADF imaging and EDX mapping of as-deposited B-overstoichiometric $Hf_{0.33-x}Al_xB_{0.67+y}$ and $Ti_{0.33-x}Al_xB_{0.67+y}$ films, performed on plan-view lamellae.

Defect formation energies decrease as the first coordination shell becomes richer in Al. Among all defects, Al vacancies exhibit the lowest formation energies in both systems, while B interstitials show the highest. Overall, the Hf-based system has lower defect formation energies than the Ti-based system. On average, Al vacancies, Hf/Ti vacancies, and B interstitials exhibit 43, 9, and 19% lower formation energies, respectively, in Hf-containing supercells. Therefore, Al vacancies are the most energetically favourable mechanism to accommodate excess B in $Hf_{0.13}Al_{0.18}B_{0.69}$.

To assess whether the presence of defects in $Hf_{0.13}Al_{0.18}B_{0.69}$ can be inferred from lattice parameter measurements, we calculated the changes in a and c upon introducing defects into a pristine $Hf_{0.16}Al_{0.17}B_{0.67}$ supercell, chosen to match the Al content of the film. The in-plane lattice parameter a is essentially insensitive; deviating by $< 0.03\%$ for all defective supercells in comparison to the pristine one. In contrast, the out-of-plane lattice parameter c is more correlated. It is

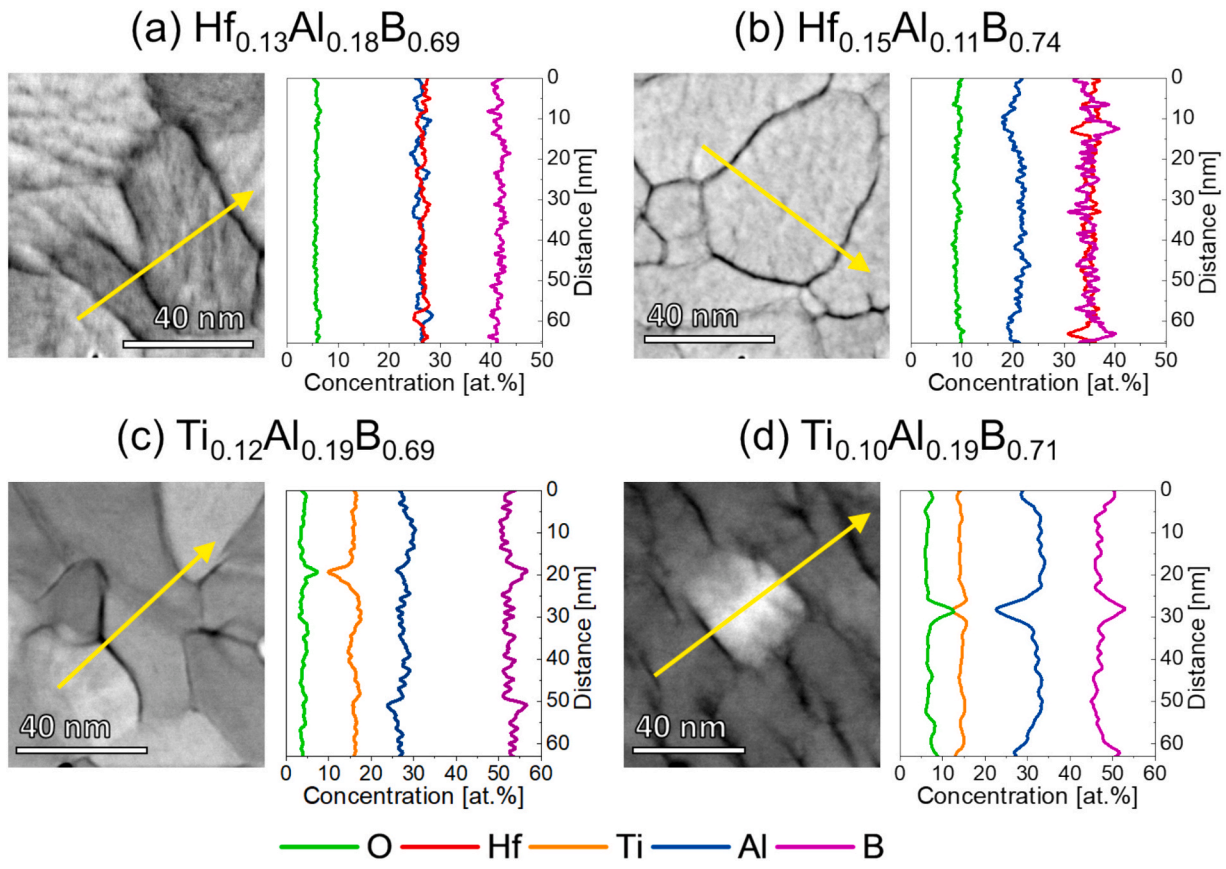

Fig. 4. EDX line scans acquired along grain boundaries and triple junctions of $Hf_{0.33-x}Al_xB_{0.67+y}$ and $Ti_{0.33-x}Al_xB_{0.67+y}$ films, measured along the arrows indicated in the corresponding STEM-HAADF micrographs.

1.56% higher compared to the pristine supercell for supercells containing a single B interstitial, but lower in those with metal vacancies, more so for the case of Hf (−0.41%) than for Al (−0.11%). Comparing with XRD-measured lattice parameters, the deviations in *c* for supercells with a singular isolated Al vacancy, Hf vacancy, and B interstitial were −0.03%, −0.33%, and +1.62%, respectively, while the corresponding deviations in *a* were −0.24%, −0.21%, and −0.25%. Meanwhile, the pristine supercell yielded deviations of +0.07% for *c* and −0.23% for *a*. While residual film stresses may introduce additional shifts in measured lattice parameters, the pronounced (0001) texture observed in most films (see Figs. S1 and S5) prevented a reliable stress analysis. However, the large positive deviation in c expected from B interstitials is difficult to reconcile with experiment regardless of plausible stress contributions. We note that this comparison only serves to narrow the plausible defect type, rather than to identify a particular lattice defect. This is reinforced by the fact that the defect concentrations in our simulated cells (~1 at. %) are still well below those required to fully account for the measured B overstoichiometry (~4 and 7 at.% for metal vacancies and B interstitials respectively) – at higher concentrations, the discrepancy for B interstitials would be still higher. Therefore, in combination with the energetics data, Al vacancies emerge as the most plausible defect type, since they best accommodate excess B, while minimally affecting c. Calculated lattice parameters for pristine Hf–Al–B supercells with varying Al content, together with defective supercells initially containing 17 at.% Al, are shown in Fig. S6.

In summary, our *ab-initio* calculations of defect energetics align with experimental observations and suggest that lower defect formation energies, particularly of Al vacancies, facilitate the incorporation of excess B within the lattice in overstoichiometric $Hf_{0.13}Al_{0.18}B_{0.69}$. As a result, the segregation of B to the grain boundaries is suppressed, in contrast to $Ti_{0.12}Al_{0.19}B_{0.69}$ and $Ti_{0.10}Al_{0.19}B_{0.71}$ where B-enriched grain boundaries lead to the formation of porous oxides consistent with literature reports, as reviewed above. However, in $Hf_{0.15}Al_{0.11}B_{0.74}$, B-enriched grain boundaries do evolve indicating that the formation of the B-rich tissue phase is retarded at lower B concentrations, but not completely suppressed in Hf-based films.

This suppression has significant technological implications: the processability of Hf-based overstoichiometric films is greatly enhanced compared to their Ti-based counterparts, as the former can accommodate higher boron concentrations, likely facilitated by Al vacancy formation, without the formation of B-rich grain boundaries. Consequently, precise control of the B-to-metal ratio during synthesis is less critical for Hf-based thin films than for Ti-based ones.

4. Conclusions

B-overstoichiometric $Hf_{0.13}Al_{0.18}B_{0.69}$ and B-understoichiometric $Hf_{0.13}Al_{0.23}B_{0.64}$ thin films formed Al-rich passivating oxide scales at 700 °C. The dense and protective oxide scale of $Hf_{0.13}Al_{0.18}B_{0.69}$ contrasts with the porous scale reported to form under similar oxidation conditions in overstoichiometric TiB_{2+y} [10,12] and $Ti_{0.10}Al_{0.19}B_{0.71}$ [17] films.

STEM and EDX analyses reveal B-enriched grain boundaries in $Ti_{0.10}Al_{0.19}B_{0.71}$, which lead to a decrease in the oxidation resistance consistent with literature. Similar boron-enriched grain boundaries were also observed in a $Ti_{0.12}Al_{0.19}B_{0.69}$ film with slightly reduced overstoichiometry. In contrast, B-overstoichiometric $Hf_{0.13}Al_{0.18}B_{0.69}$ showed no B-enrichment at the grain boundaries.

Ab initio calculations indicate that excess B is more easily accommodated as lattice defects in Hf-based films compared to Ti-based ones. Systematic calculations of the local chemical environment-dependent formation energies of selected lattice defects indicate 43, 9, and 19%

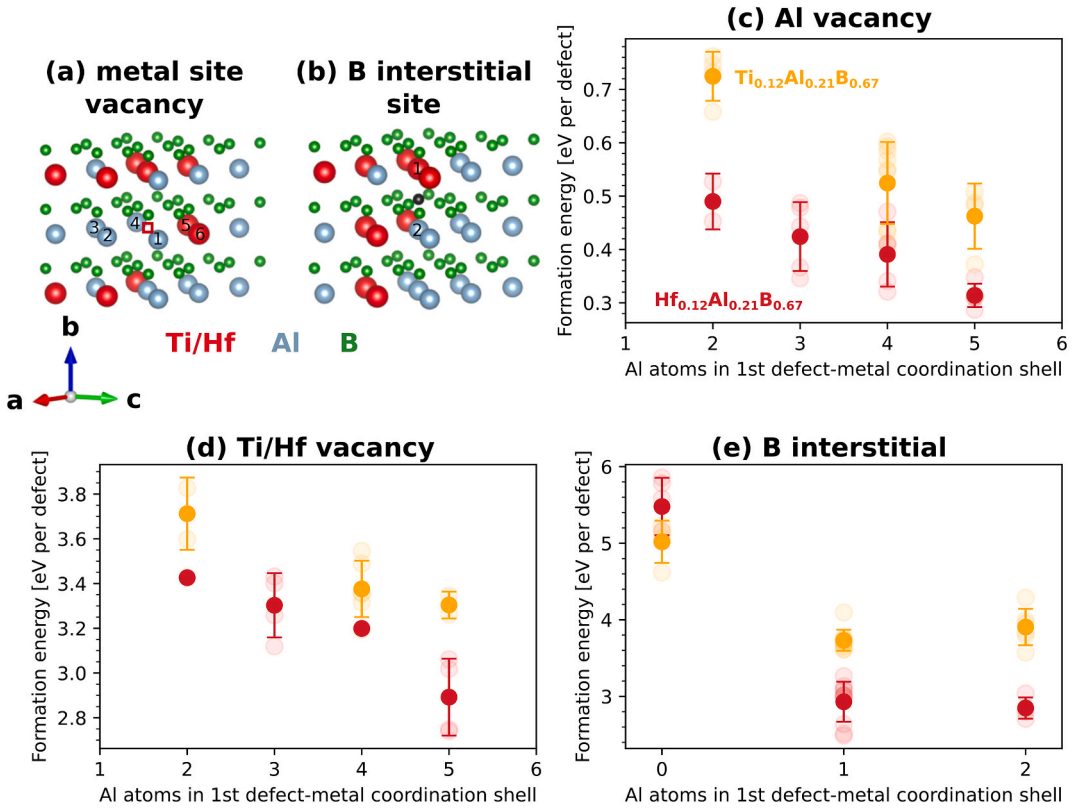

Fig. 5. Ab-initio calculated defect energetics for $Hf_{0.12}Al_{0.21}B_{0.67}$ and $Ti_{0.12}Al_{0.21}B_{0.67}$ depending on the local chemical environment. Schematic of the considered defects in representative SQS supercells – (a) metal vacancy marked with a red square and (b) B interstitial, highlighted in black. Atoms in the 1st metal-defect coordination shells are numbered. Formation energies of (c) Al vacancies, (d) Ti/Hf vacancies, and (e) B interstitials as a function of the number of Al atoms in the 1st metal-defect co-ordination shell.

lower formation energies, respectively, for Al vacancies, transition metal vacancies, and B interstitials in the Hf-Al-B system compared to the Ti-Al-B system. Al vacancies show the largest relative reduction and are the most energetically favorable defects in both systems. The formation of a tissue phase in $Hf_{0.13}Al_{0.18}B_{0.69}$ is therefore suppressed via the formation of such defects, particularly Al vacancies. However, for $Hf_{0.15}Al_{0.11}B_{0.74}$, B segregation at the grain boundary is observed, indicating that it is entirely suppressed only at lower B concentrations via defect formation.

To critically appraise this hypothesis for $Hf_{0.13}Al_{0.18}B_{0.69}$, the lattice parameters were determined by DFT for pristine and defect-containing supercells and compared to XRD measurements. Although the in-plane lattice parameter *a* shows comparable deviation in all cases, the experimental *c* value is most consistent with Al vacancies. This agreement, along with their lowest energetic barrier for defect formation, suggests that Al vacancies are the most plausible defect structure to retard the formation of the B-rich tissue phase at lower B concentrations.

Hence, the processability of Hf-based films is significantly improved, as they can accommodate higher concentrations of B, likely due to Al vacancy formation, without forming B-rich grain boundaries, unlike Ti-based overstoichiometric films. This reduces the need for strict control of the B-to-metal ratio during synthesis for Hf-based thin films, which is required for the Ti-based films.

CRediT authorship contribution statement

Sameer Aman Salman: Writing – review & editing, Writing – original draft, Visualization, Methodology, Investigation, Formal analysis, Data curation, Conceptualization. **Pauline Kümmerl:** Writing – review & editing, Writing – original draft, Visualization, Methodology, Investigation, Formal analysis, Data curation, Conceptualization. **Sebastian Lellig:** Writing – review & editing, Validation, Investigation, Formal analysis. **Amir Hossein Navidi Kashani:** Writing – review & editing, Validation, Resources, Methodology, Formal analysis. **Devi Janani Ramesh:** Writing – review & editing, Validation, Methodology, Investigation, Formal analysis. **Eva B. Mayer:** Writing – review & editing, Validation, Resources, Investigation. **Stanislav Mráz:** Writing – review & editing, Validation, Methodology. **Marcus Hans:** Writing – review & editing, Validation, Investigation, Formal analysis. **Daniel Primetzhofer:** Writing – review & editing, Validation, Investigation, Funding acquisition, Formal analysis. **Szilárd Kolozsvári:** Writing – review & editing, Resources. **Peter Polcik:** Writing – review & editing, Resources. **Johann Michler:** Writing – review & editing, Validation, Resources, Funding acquisition. **Jochen M. Schneider:** Writing – review & editing, Writing – original draft, Validation, Supervision, Resources, Project administration, Funding acquisition, Conceptualization.

Declaration of competing interest

The authors declare that they have no known competing financial interests or personal relationships that could have appeared to influence the work reported in this paper.

Acknowledgements

This research was funded by German Research Foundation (Project Number 506336880). Transnational ion beam analysis access has been supported by the RADIATE project under the Grant Agreement 824096 from the EU Research and Innovation program HORIZON 2020. Accelerator operation at Uppsala University has been supported by the Swedish research council VR-RFI (#2019-00191 & 2023-00155). We gratefully acknowledge the computing time provided to us on the HPC

cluster CLAIX at the NHR Center NHR4CES with project id p0020883.

Appendix A. Supplementary data

Supplementary data to this article can be found online at https://doi.org/10.1016/j.matdes.2026.115920.

Data availability

Data will be made available on request.

References

[1] G. Akopov, M.T. Yeung, R.B. Kaner, Rediscovering the Crystal Chemistry of Borides, Adv. Mater. 29 (2017) 1604506, https://doi.org/10.1002/adma.201604506.

[2] C. Feldman, F.G. Satkiewicz, N.A. Blum, The behavior of TiB2 thin film electrodes in polycrystalline silicon thin film solar cells, Journal of the Less Common Metals 82 (1981) 183–191, https://doi.org/10.1016/0022-5088(81)90218-6.

[3] J.W. Zimmermann, G.E. Hilmas, W.G. Fahrenholtz, R.B. Dinwiddie, W.D. Porter, H. Wang, Thermophysical Properties of ZrB2 and ZrB2–SiC Ceramics, J. Am. Ceram. Soc. 91 (2008) 1405–1411, https://doi.org/10.1111/j.1551-2916.2008.02268.x.

[4] L. Tengdelius, J. Birch, J. Lu, L. Hultman, U. Forsberg, E. Janzén, H. Högberg, Magnetron sputtering of epitaxial ZrB2 thin films on 4H-SiC(0001) and Si(111), Physica Status Solidi (a) 211 (2014) 636–640, https://doi.org/10.1002/pssa.201330308.

[5] J. Sung, D.M. Goedde, G.S. Girolami, J.R. Abelson, Remote-plasma chemical vapor deposition of conformal ZrB2 films at low temperature: a promising diffusion barrier for ultralarge scale integrated electronics, J. Appl. Phys. 91 (2002) 3904–3911, https://doi.org/10.1063/1.1436296.

[6] Y.-H. Koh, S.-Y. Lee, H.-E. Kim, Oxidation Behavior of Titanium Boride at Elevated Temperatures, J. Am. Ceram. Soc. 84 (2001) 239–241, https://doi.org/10.1111/j.1151-2916.2001.tb00641.x.

[7] T.A. Parthasarathy, R.A. Rapp, M. Opeka, R.J. Kerans, A model for the oxidation of ZrB2, HfB2 and TiB2, Acta Mater. 55 (2007) 5999–6010, https://doi.org/10.1016/j.actamat.2007.07.027.

[8] W.G. Fahrenholtz, G.E. Hilmas, Oxidation of ultra-high temperature transition metal diboride ceramics, Int. Mater. Rev. 57 (2012) 61–72, https://doi.org/10.1179/1743280411Y.0000000012.

[9] N. Schalk, M. Tkadletz, C. Mitterer, Hard coatings for cutting applications: Physical vs. chemical vapor deposition and future challenges for the coatings community, Surface and Coatings Technology 429 (2022) 127949, https://doi.org/10.1016/j.surfcoat.2021.127949.

[10] S. Dorri, J. Palisaitis, G. Greczynski, I. Petrov, J. Birch, L. Hultman, B. Bakhit, Oxidation kinetics of overstoichiometric TiB2 thin films grown by DC magnetron sputtering, Corros. Sci. 206 (2022) 110493, https://doi.org/10.1016/j.corsci.2022.110493.

[11] B. Bakhit, J. Palisaitis, J. Thörnberg, J. Rosen, P.O.Å. Persson, L. Hultman, I. Petrov, J.E. Greene, G. Greczynski, Improving the high-temperature oxidation resistance of TiB2 thin films by alloying with Al, Acta Mater. 196 (2020) 677–689, https://doi.org/10.1016/j.actamat.2020.07.025.

[12] J. Thörnberg, B. Bakhit, J. Palisaitis, N. Hellgren, L. Hultman, G. Greczynski, P.O. Å. Persson, I. Petrov, J. Rosen, Improved oxidation properties from a reduced B content in sputter-deposited TiBx thin films, Surf. Coat. Technol. 420 (2021) 127353, https://doi.org/10.1016/j.surfcoat.2021.127353.

[13] C. Fuger, R. Hahn, A. Hirle, T. Wojcik, P. Kutrowatz, F. Bohrn, O. Hunold, P. Polcik, H. Riedl, Tissue phase affected fracture toughness of nano-columnar TiB2 + z thin films, Materials Research Letters 11 (2023) 613–622, https://doi.org/10.1080/21663831.2023.2204120.

[14] N. Nedfors, A. Mockute, J. Palisaitis, P.O.Å. Persson, L.-Å. Näslund, J. Rosen, Influence of pulse frequency and bias on microstructure and mechanical properties of TiB2 coatings deposited by high power impulse magnetron sputtering, Surf. Coat. Technol. 304 (2016) 203–210, https://doi.org/10.1016/j.surfcoat.2016.06.086.

[15] P. Kümmerl, S. Lellig, A.H. Navidi Kashani, M. Hans, P.J. Pöllmann, L. Löfler, G. K. Nayak, D.M. Holzapfel, S. Kolozsvári, P. Polcik, P. Schweizer, D. Primetzhofer, J. Michler, J.M. Schneider, Improved oxidation behavior of Hf0.11Al0.20B0.69 in comparison to Hf0.28B0.72 magnetron sputtered thin films, Sci. Rep. 14 (2024) 21653, https://doi.org/10.1038/s41598-024-72134-3.

[16] A.H. Navidi Kashani, M. Hans, S. Lellig, D.M. Holzapfel, L. Löfler, S. Mráz, D. Primetzhofer, J. Michler, J.M. Schneider, Morphology, mechanical properties, and oxidation behavior of stoichiometric Ti0.33-xAlxB0.67 coatings (x = 0.04, 0.15, 0.21, and 0.28), Acta Materialia 270 (2024) 119829. https://doi.org/10.1016/j.actamat.2024.119829.

[17] A.H. Navidi Kashani, S. Mráz, D.M. Holzapfel, M. Hans, L. Löfler, P. Ondračka, D. Primetzhofer, J.M. Schneider, Synthesis and oxidation behavior of Ti0.35Al0.65By (y = 1.7–2.4) coatings, Surface and Coatings Technology 442 (2022) 128190, https://doi.org/10.1016/j.surfcoat.2022.128190.

[18] J. Neidhardt, S. Mráz, J.M. Schneider, E. Strub, W. Bohne, B. Liedke, W. Möller, C. Mitterer, Experiment and simulation of the compositional evolution of Ti–B thin films deposited by sputtering of a compound target, J. Appl. Phys. 104 (2008) 063304, https://doi.org/10.1063/1.2978211.

[19] M. Ohring, Chapter 9 - Film Structure, in: M. Ohring (Ed.), Materials Science of Thin Films (second Edition), Academic Press, San Diego, 2002, pp. 495–558, https://doi.org/10.1016/B978-012524975-1/50012-4.

[20] J. Thörnberg, J. Palisaitis, N. Hellgren, F.F. Klimashin, N. Ghafoor, I. Zhirkov, C. Azina, J.-L. Battaglia, A. Kusiak, M.A. Sortica, J.E. Greene, L. Hultman, I. Petrov, P.O.Å. Persson, J. Rosen, Microstructure and materials properties of understoichiometric TiBx thin films grown by HiPIMS, Surf. Coat. Technol. 404 (2020) 126537, https://doi.org/10.1016/j.surfcoat.2020.126537.

[21] J. Emmerlich, S. Mráz, R. Snyders, K. Jiang, J.M. Schneider, The physical reason for the apparently low deposition rate during high-power pulsed magnetron sputtering, Vacuum 82 (2008) 867–870, https://doi.org/10.1016/j.vacuum.2007.10.011.

[22] P. Ström, D. Primetzhofer, Ion beam tools for nondestructive in-situ and in-operando composition analysis and modification of materials at the Tandem Laboratory in Uppsala, J. Inst. 17 (2022) P04011, https://doi.org/10.1088/1748-0221/17/04/P04011.

[23] P. Ström, P. Petersson, M. Rubel, G. Possnert, A combined segmented anode gas ionization chamber and time-of-flight detector for heavy ion elastic recoil detection analysis, Rev. Sci. Instrum. 87 (2016) 103303, https://doi.org/10.1063/1.4963709.

[24] E. Pitthan, M.V. Moro, S.A. Corrêa, D. Primetzhofer, Assessing boron quantification and depth profiling of different boride materials using ion beams, Surf. Coat. Technol. 417 (2021) 127188, https://doi.org/10.1016/j.surfcoat.2021.127188.

[25] B. Bakhit, D. Primetzhofer, E. Pitthan, M.A. Sortica, E. Ntemou, J. Rosen, L. Hultman, I. Petrov, G. Greczynski, Systematic compositional analysis of sputter-deposited boron-containing thin films, J. Vac. Sci. Technol. A 39 (2021) 063408, https://doi.org/10.1116/6.0001234.

[26] P. Hohenberg, W. Kohn, Inhomogeneous Electron Gas, Phys. Rev. 136 (1964) B864–B871, https://doi.org/10.1103/PhysRev.136.B864.

[27] G. Kresse, J. Hafner, Ab initio molecular dynamics for open-shell transition metals, Phys. Rev. B 48 (1993) 13115–13118, https://doi.org/10.1103/PhysRevB.48.13115.

[28] G. Kresse, J. Hafner, Ab initio molecular-dynamics simulation of the liquid-metal–amorphous-semiconductor transition in germanium, Phys. Rev. B 49 (1994) 14251–14269, https://doi.org/10.1103/PhysRevB.49.14251.

[29] G. Kresse, D. Joubert, From ultrasoft pseudopotentials to the projector augmented-wave method, Phys. Rev. B 59 (1999) 1758–1775, https://doi.org/10.1103/PhysRevB.59.1758.

[30] J.P. Perdew, K. Burke, M. Ernzerhof, Generalized Gradient Approximation made simple, Phys. Rev. Lett. 77 (1996) 3865–3868, https://doi.org/10.1103/PhysRevLett.77.3865.

[31] H.J. Monkhorst, J.D. Pack, Special points for Brillouin-zone integrations, Phys. Rev. B 13 (1976) 5188–5192, https://doi.org/10.1103/PhysRevB.13.5188.

[32] D. Gehringer, M. Friák, D. Holec, Models of configurationally-complex alloys made simple, Comput. Phys. Commun. 286 (2023) 108664, https://doi.org/10.1016/j.cpc.2023.108664.

[33] S. Lellig, A.H. Navidi Kashani, P. Schweizer, M. Hans, G.K. Nayak, J. Michler, J.M. Schneider, Passivating oxidation behavior of Ti0.12Al0.21B0.67 coatings investigated by scanning transmission electron microscopy and chemical environment dependent density functional theory simulations, Acta Materialia 285 (2025) 120662. https://doi.org/10.1016/j.actamat.2024.120662.

[34] D.J. Tallman, B. Anasori, M.W. Barsoum, A critical Review of the Oxidation of Ti2AlC, Ti3AlC2 and Cr2AlC in Air, Materials Research Letters 1 (2013) 115–125, https://doi.org/10.1080/21663831.2013.806364.

[35] D.M. Holzapfel, D. Music, M. Hans, S. Wolff-Goodrich, D. Holec, D. Bogdanovski, M. Arndt, A.O. Eriksson, K. Yalamanchili, D. Primetzhofer, C.H. Liebscher, J. M. Schneider, Enhanced thermal stability of (Ti,Al)N coatings by oxygen incorporation, Acta Mater. 218 (2021) 117204, https://doi.org/10.1016/j.actamat.2021.117204.

[36] G.K. Nayak, D. Holec, J.M. Schneider, Vacancy-concentration-dependent thermal stability of fcc-(Ti,Al)Nx predicted via chemical-environment-sensitive diffusion activation energies, arXiv.Org (2025). https://arxiv.org/abs/2510.16467v1 (accessed November 13, 2025).